IEEE Access
Multidisciplinary | Rapid Review | Open Access Journal

Received July 28, 2021, accepted August 8, 2021, date of publication August 12, 2021, date of current version August 18, 2021.

Digital Object Identifier 10.1109/ACCESS.2021.3104511

Dual-Functional Ultrawideband Antenna With High Fidelity Factor for Body Area Networks and Microwave Imaging Systems

ZAHRA LASEMIIMENI[1], ZAHRA ATLASBAF[1], (Senior Member, IEEE), AND NIMA KARBASCHI[2]

[1]Department of Electrical and Computer Engineering, Tarbiat Modares University, Tehran 14115-111, Iran
[2]Department of Electrical and Computer Engineering, Babol Noshirvani University of Technology, Babol 47148-71167, Iran

Corresponding author: Zahra Lasemiimeni (z.lasemi@modares.ac.ir)

ABSTRACT Microwave Imaging (MI) and Body Area Networks (BANs) technologies are widely used in healthcare systems. A dual-functional compact ultrawideband (UWB) antenna with a high on-body and off-body fidelity factor is presented in this paper. The antenna's design approach is based on analyzing the return loss, the antenna's gain, the phase of S_{21}, and the group delay over the UWB frequency band, in each designing step, to achieve the highest level of fidelity factor in both E- and H-plane. The final design (Ant. 3) consists of a circular ring with six intersecting rings in the radiating element and an elliptic ground plane with an overall size of $16 \times 20\ mm^2$. Simulated and experimental evaluations both in free space and on-body prove the excellent operation of Ant. 3 within the FCC UWB bandwidth of 3.1 to 10.6 GHz in terms of return loss and fidelity factor (greater than 0.9 at all angles). For body area communication, the final design presents the fidelity factor greater than 0.93 near the human arm. Also, for breast cancer detection applicability, a 12-element array of Ant. 3 is located around a conical breast model. The results show the antenna's promising performance in detecting 6-mm average diameter malignant tumor and 3-mm average diameter benign tumor.

INDEX TERMS Fidelity factor, microwave imaging, pulse preserving capabilities, ultrawideband (UWB), breast cancer detection, body area network (BANs).

I. INTRODUCTION

UWB technology is vastly in use in plenty of industries and applications. One of the applications that have become widespread these days is healthcare imaging and monitoring. MI technology and BANs attracted attention in the UWB healthcare applications, in which the antenna design plays a critical role [1]–[7]. Nowadays, many women around the world suffer from breast cancer. The nonionizing microwave breast imaging can be exploited as a potential alternative imaging method for the detection of earliest stage tumors. In this case, UWB radar-based imaging technology identifies and localizes noticeable scattering signatures by utilizing short UWB electromagnetic pulses [8], [9]. The large bandwidths of these pulses are beneficial both in penetrating sufficiently in-depth (in the lower range of bandwidth) and providing better range resolution (in the higher range of the bandwidth) [10].

The BANs are a branch of wireless systems, which are located on the body. They also work as wearable gadgets, which their main objective is to establish a link between the human body and electronic devices. Nowadays, BANs are utilized for wearable applications in sports, biomedical engineering, and the military [11]–[14]. In BAN systems, the antenna has some requirements to guarantee the reliability of the whole system. For instance, the antenna should be low profile, small in size, and the polarization should be normal to the body surface [15]. Besides, the antennas should work well in the vicinity of the body (on-body), and also far from the body (off-body) [7], [14].

BANs and UWB radar-based imaging technologies transmit short UWB electromagnetic pulses, which can greatly be affected by distortion [14], [16], [17]. In the time domain, the distortion that an antenna adds to a signal at different angles and distances can be quantified by utilizing

The associate editor coordinating the review of this manuscript and approving it for publication was Tae Wook Kim.

TABLE 1. Comparison with other UWB antennas from literature.

Ref. no	Dimension (mm^2)	Application	BW (GHz)	Fidelity Factor	Evaluation Regions
[10]	20x20	MI	2-4	0.61 to 0.92 **Average**= 0.785	-90° to $+90^{\circ}$
[12]	30x30 (Three different Sine-Gaussian pulses)	BANs	3.2-10	**Free Space** = 0.96, 0.98, 0.99 **On Body** > 0.95	**Only at the Boresight of the antenna**
[13]	80x61 (Three different Rayleigh pulses)	BANs	3.18-11	**Free Space**= 0.968, 0.994, 0.996 **On Body**= 0.952, 0.993, 0.996	**Only at the Boresight of the antenna**
[14]	80x67 (Signal I, II)	BANs	3.7-10.3	**Free Space:** 0.72, 0.77 **On Body**: 0.68, 0.79	**Only at the Boresight of the antenna**
[16]	16x22 (Signal I, Signal II)	MI	2.95-12	**E-plane** / **H-plane** **Far-field:** 0.86 to 0.99 / 0.98 to 0.99 **Near-field:** 0.85 to 0.99 / 0.96 to 0.99	-180° to $+180^{\circ}$
[26]	34x67	MI	4-16	**Not Evaluated**	-
[27]	33.14x14.9	BANs and MI	3.1-11	**Not Evaluated**	-
[29]	51.6x51.6 (Sine-Gaussian)	MI	1.6-7.1	**Far-field** / **Near-field** 0.65 to 0.95 / 0.75 to 0.95	-70° to $+70^{\circ}$
Our work	16x20 (Signal I, Signal II)	BANs and MI	3-12	**E-plane** / **H-plane** **Far-field:** 0.9 to 0.99 / 0.98 to 0.99 **Near-field:** 0.92 to 0.99 / 0.96 to 0.99 **On Body**: 0.93 to 0.99 / 0.97 to 0.99 --- **In Body**: 0.94 to 0.99	-180° to $+180^{\circ}$

the fidelity parameter [18]. Furthermore, in the frequency domain, the total phase distortion of the antenna system is measured by group delay that is a derivative of the transfer function's phase versus angular frequency. The high variation in group delay means the frequency components of the transmitted signals are not received efficiently and equally, and consequently, distortion in the time-domain received signals occurs. However, the only parameter that quantitatively calculates the distortion in terms of time, space, and frequency is the fidelity factor [16], [17], [19]. In addition to the radiation parameters of antennas, [16] analytically shows that the fidelity factor is one of the most important parameters for evaluating the antenna that is utilized in radar-based applications. [20] explains that the fidelity value above 0.9 is suitable for radar-based applications.

To date, numerous unidirectional antenna designs have been reported for radar-based UWB microwave breast imaging, e.g., the spiral antenna [21], ridged pyramidal horn [22], balanced antipodal Vivaldi antenna [23], and bowtie antenna [24]. The large axial lengths of these antennas increase the overall size of the imaging system in practical scenarios [25]. Recently, planar printed monopole antennas have been considered for breast cancer screening systems [10], [16], [25]–[27] because of their merits such as simple and low-cost structure, low profile, wide impedance bandwidth, and ease of fabrication. Additionally, designing a low profile and small-size antenna would also enable a higher number of antenna elements around the tissue; thus, more received signals can be exploited, and resolution would be enhanced [10].

This paper's main novelty is to design a compact antenna with a high fidelity factor, suitable for two important applications of healthcare systems, namely MI and BANs. This antenna has a wide bandwidth on the body (3 to 12 GHz) and can send body signature signals with a pulse preserving capability of more than 0.93. It can also detect a 6-mm average diameter malignant tumor and a 3-mm diameter benign tumor with a fidelity factor of more than 0.94 in breast tissue.

The printed monopole antennas, already presented for breast imaging, are relatively larger than our via-fed antenna [26], [27] or, with a similar size to our antenna, have less bandwidth or pulse preserving capability [10], [16]. [27] presents a large size CPW monopole antenna for UWB body-centric imaging applications. However, [27] does not evaluate any of the time- or frequency-domain distortion analyses. Additionally, the return loss performance of the CPW monopole antenna is evaluated in the proximity of a non-dispersive, flat-layered arm model. This simple characterization of the body tissue leads to less accurate predictions of the antenna parameters in the UWB frequency range. Compared to [16], our via-fed antenna has distinguishing features. Firstly, the fidelity factor values are increased to more than 0.9 in all angles. Additionally, with an imaging system configuration similar to [16], the 3-mm diameter spherical benign tumor is detected with our proposed antenna; however, we did not manage to detect this size of the tumor with the antenna in [16]. Also, our proposed via-fed antenna has been tested in BAN applications, and thus the multi-function capability has been confirmed. [28] utilizes a complex natural responses (CNRs) method to discriminate between benign and malignant tumors. A 10-mm spherical benign tumor and a 10-mm average diameter malignant tumor are detected by a mono-static imaging system that uses a single Vivaldi antenna. By our proposed via-fed antenna, a 40 percent reduction in the size of the detected tumors is achieved so that a 6-mm average diameter malignant tumor and 3-mm spherical tumors are diagnosed here. In Table 1, we show our via-fed antenna's superiority in terms of

bandwidth, physical dimension, fidelity factor value, and fidelity factor evaluation regions over some of the published UWB antennas in the literature [10], [12]–[14], [16], [26], [27], [29].

The rest of the paper is organized as follows. In section II, the antenna design and geometry are presented, where its fidelity factor is evaluated in the far-field with two different input signals. To clarify the antenna performance the results of the parametric study are exhibited. The antenna's dual-function applicability in BAN technology and breast imaging system is studied in section III. The antenna performance in the vicinity of the arm is described from the viewpoint of S_{11} and the fidelity factor. Also, the microwave imaging capabilities in tumor detection and localization are assessed, and imaging results show that this antenna is a suitable candidate for breast cancer detection. Finally, our paper is concluded in section IV.

II. ANTENNA DESIGN AND MEASUREMENT

A. PERFORMANCE PARAMETERS

The fidelity factor is a system-dependent parameter that depends not only on the input signal waveform but also on the antenna characteristics such as the transfer function, gain, and return loss performance [17], [19], [30]. If the antenna excitation signal spectrum is in the frequency ranges that the magnitude of antenna return loss is more than -10 dB, the fidelity factor values decrease [14]. [16] utilizes Friis' transmission equation to show that time- and frequency-domain antenna distortion characteristics (group delay and fidelity factor, respectively) are interdependent criteria. To have a group delay with minimum fluctuations in the frequency domain and a high-fidelity parameter in the time domain, the antenna transfer function is required to have a flat magnitude [16], [17], [19]. Based on Friis's equation, the gain should have an increasing trend with an increase in frequency to have a flat transfer function. Therefore, in addition to return loss performance, the flow of changes in gain is an important factor in determining antenna distortion behavior [16].

Here, the return loss, gain, and group delay are investigated in each antenna designing stage to design a high-fidelity antenna suitable for UWB radar-based applications. The fidelity parameter is defined as the maximum cross-correlation of $\hat{S}_R(t)$, normalized electric field intensity signals observed at virtual probes and $\hat{S}_T(t)$, the normalized input signal. It is calculated as follows [31]:

$$FF = \max_{\tau} \left\{ \int_{-\infty}^{\infty} \hat{S}_T(t)\, \hat{S}_R(t+\tau) dt \right\} \tag{1}$$

To properly evaluate the antenna distortion effect, one should choose a signal whose pulse spectrum is almost entirely located in the operating bandwidth of the antenna system. In this paper, to calculate the fidelity factor, two different signals are generated as the antenna input signal. The first one is the Gaussian pulse and is generated in CST as a default signal that covers the UWB standard bandwidth (3.1-10.6 GHz). The second is the sine-modulated Gaussian pulse that has the following pulse parameter $f_c = 7$ GHz, $b = 220$ *ps* [16]. Fig. 1 illustrates the plot of the normalized input signals (The CST generated signal and the sine-modulated Gaussian pulse are called Signal I and Signal II, respectively in this paper) along with their spectrum amplitudes. In this study, the fidelity factor is calculated in both E-plane and H-plane as a function of the angle, away from boresight. There are 36 virtual probes placed in both planes in the far-field and near-field regions of the transmitting antenna. These probes are located every 10° from 0° to 350° on a circular path centered at the center point of the antenna.

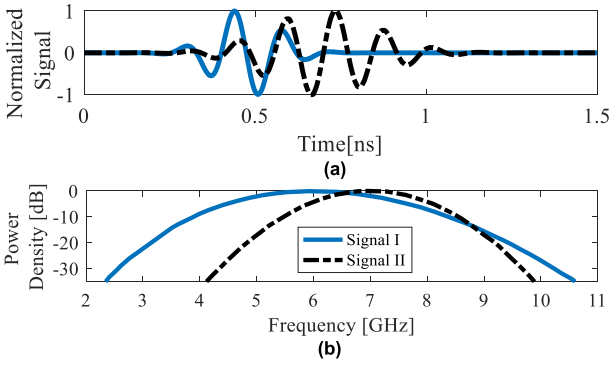

FIGURE 1. (a) Time-domain waveform of the input signals and (b) spectrum amplitude of the input signals.

B. DESIGN STAGES

The UWB antenna with pulse preserving capabilities in all directions of E-plane and H-plane for healthcare applications is designed here. The antenna's structure is changed in a three-step evolution process to improve return loss and achieve an increasing trend for the gain and a constant group delay over the UWB frequency range.

The primary structure of the antenna shown in Fig. 2 (a) consists of a circular ring radiator with an outer radius of R_1 and an inner radius of R_2 designed on a low-cost FR4 substrate with a thickness of 1.6 mm and is fed by a 50-ohm microstrip line placed on its top layer. The ground plane of this antenna is semi-elliptic, with a major axis of l_g and a ratio of 0.75.

Secondly, as shown in Fig. 2 (b), six rings which are the scaled version of the larger ring with the scaling factor of $R_1/r_1 = 3$ are inserted inside the circular ring radiator of the first step. The addition of the six intersecting rings creates different current paths in the middle of the structure, which leads to the generation of additional resonant frequencies and, consequently, the improvement of the return loss. The values of the other design parameters are as follows: $W = 16$ mm, $L = 20$ mm, $R_1 = 6$ mm, $R_2 = 5$ mm, $r_1 = 2$ mm, $r_2 = 1.5$ mm, $d = 3.1$ mm, $l_g = 16$ mm, $h_g = 6$ mm, and $h_f = 9$ mm.

For the last step, the ground plane's position is changed, and the microstrip line feeds the antenna on the bottom side

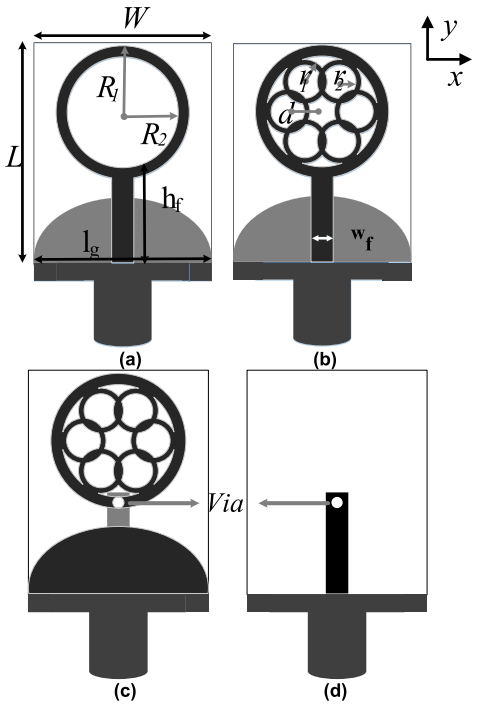

FIGURE 2. Evolution of the via-fed UWB antenna (a) Ant. 1, (b) Ant. 2 (c) Ant. 3: the via-fed antenna (front view), and (d) Ant. 3 (back view).

of the substrate through a via. Since our proposed antenna is compact, this feeding technique is applied to broaden the antenna bandwidth (see Fig. 2 (c)) [32]. The diameter of the metalized via is 1 mm. The simulation results of this section are performed in free space.

The simulated return loss, gain, phase of S_{21}, and group delay of the designed antenna structures in the evolution process are presented in Figs. 3-5, respectively. As shown in Fig. 3, although Ant. 1 represents a good performance at the lower edge of the bandwidth, the antenna does not have an acceptable impedance matching in the middle frequencies. The simulation results also reveal that these six elements generate a resonant frequency at 7.25 GHz and significantly improve the return loss in the middle frequencies. However, in the upper frequency of the bandwidth, the impedance matching issue comes up.

Fig. 4 shows that the gain of Ant. 1 noticeably drops in the frequency range of 9-11 GHz. Although the downward trend of the gain in Ant. 1 is compensated in Ant. 2, the antenna gain has a negative slope in the frequency range of 7-9 GHz. As Fig. 5 (a) shows, the non-linear phase of S_{21} occurs in the frequency ranges that the antennas aren't matched and their gains have a negative slope.

For Ant. 1 and Ant. 2, regarding return loss performances, the excitation signals' energy is distributed outside the operating bandwidth of the antennas, and also, the gain does not increase with the decline in the wavelength. Consequently, parts of the signals' frequency content are filtered out, and a considerable group delay variation in the frequency domain

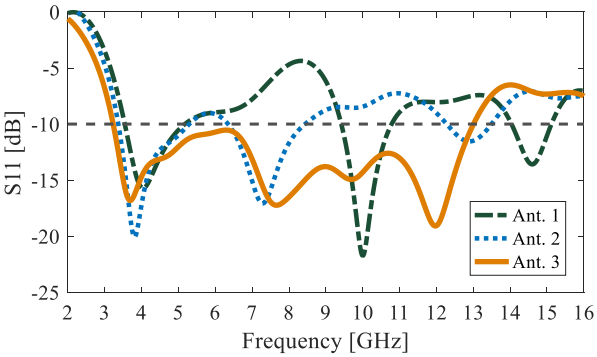

FIGURE 3. Simulated return loss performance of the antennas.

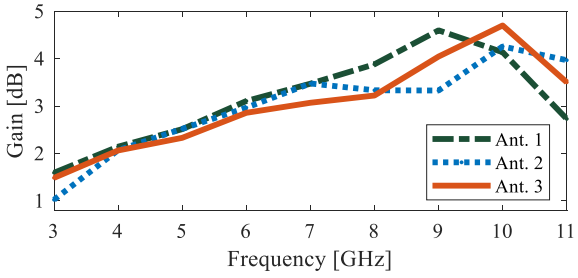

FIGURE 4. Simulated gain of the antennas versus frequency.

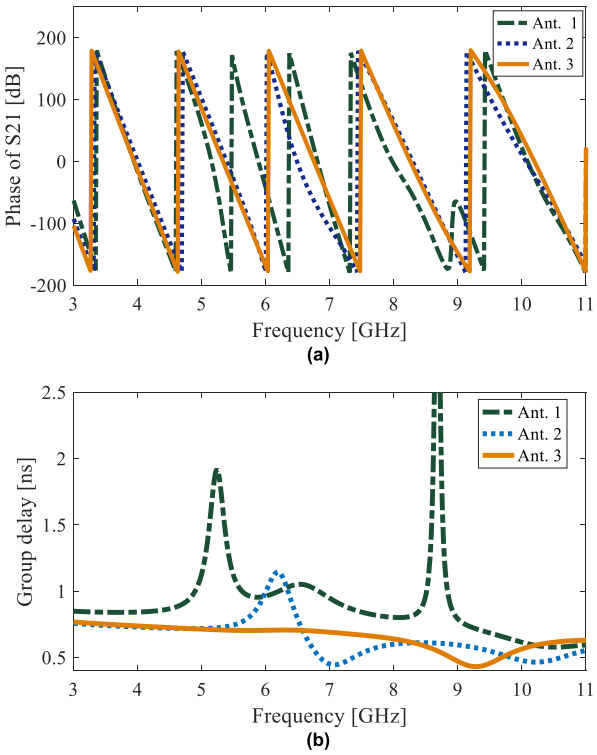

FIGURE 5. (a) phase of S21 and (b) group delay of the simulated antennas.

occurred, which imposes distortions to the time-domain signals. The group delays fluctuation of Ant. 1 and Ant. 2 are 3.56 ns and 0.67 ns, respectively.

In the last structure, S_{11} is improved in the upper frequency of bandwidth (8-13 GHz). The magnitude of antenna return

loss is less than −10 dB in the whole UWB frequency range. Finally, an increasing trend for gain over the UWB range along with a liner phase of S_{21}(except for the 10-10.6 GHz frequency band) is achieved. As Fig. 5 (b) demonstrates, the final design has a nearly constant group delay that has an insignificant fluctuation (0.4 ns) in the upper frequency of the band. This fluctuation originates from the non-linear phase of S_{21} in the upper frequency of the UWB frequency range.

To quantify the level of distortion, Figs. 6 and 7 show the far-field fidelity factor of the designated antennas, in all directions of E-plane and H-plane. As expected, a significant improvement in fidelity factor is achieved in Ant. 2, comparing Ant. 1 (Figs. 6 and 7). Nevertheless, this improvement is not still satisfying the merits of radar-based systems [20].

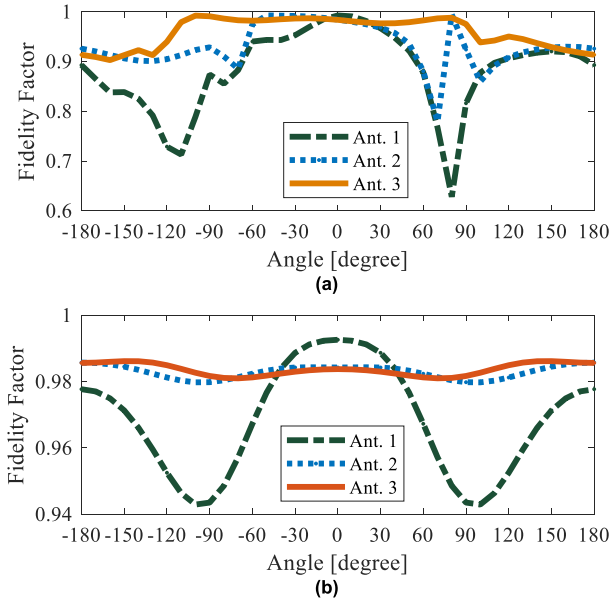

FIGURE 6. Calculated far-field fidelity factor of the antennas in (a) E-plane (y-z) and (b) H-plane (x-z) with signal I input.

By comparing the far-field fidelity values presented in Table 2, a significant improvement can be seen in Ant. 3, with respect to Ant. 1 and Ant. 2. The fidelity factor of Ant. 3 is greater than 0.9 in all directions. As can be seen in Fig. 1 (b), the spectrum of Signal II is slightly more centralized in our considered bandwidth, thus having more frequency components, comparing to Signal I. Therefore, the slight deviation appeared due to the diversity of these two pulses' spectrum [14], [16], [30].

C. DESIGN ANALYSIS OF THE PROPOSED ANTENNA

In designing the antenna, the lower frequency f_L is calculated by [33]:

$$f_L = \frac{c}{2 \times 2.\frac{A}{r}.\sqrt{\varepsilon_{eff}}} \tag{2}$$

$$\varepsilon_{eff} = \frac{\varepsilon_r + 1}{2} + \frac{\varepsilon_r - 1}{2}\left[1 + 12\frac{h}{w_f}\right]^{-\frac{1}{2}} \tag{3}$$

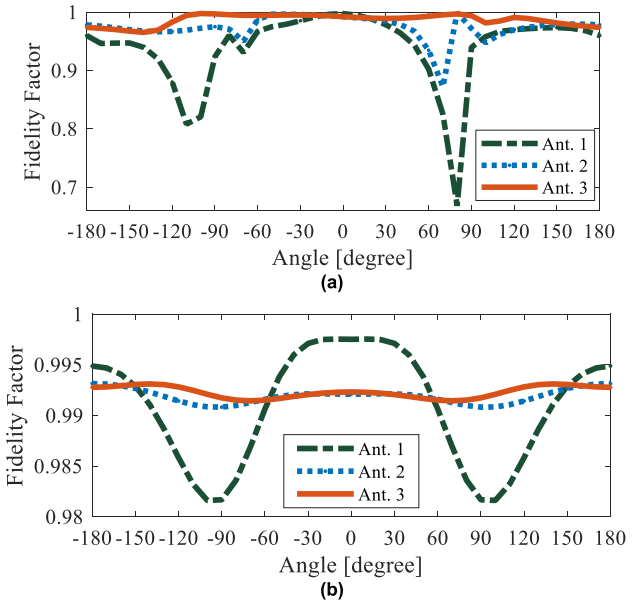

FIGURE 7. Calculated far-field fidelity factor of the antennas in (a) E-plane (y-z) and (b) H-plane (x-z) with signal II input.

TABLE 2. Far-field fidelity factor of Ant. 1, Ant. 2, and Ant. 3.

Input		Ant. 1	Ant. 2	Ant. 3
Signal I	H-P	0.943-0.993	0.98-0.986	0.981-0.986
	E-P	0.628-0.993	0.779-0.995	0.901-0.992
Signal II	H-P	0.982-0.998	0.991-0.993	0.991-0.993
	E-P	0.668-0.998	0.872-0.999	0.965-0.998

where c is the speed of light, A is the area of the patch, h is the thickness of the substrate, and ε_{eff} is the effective dielectric constant. [33] considers r equal to the outer radius of the central patch. However, if the antenna includes a slot, r will be the radius of a circle, whose area is equal to A.

As Fig. 8 (a) shows, the antenna patch comprises two intersecting areas: S_P (the purple area) and S_R (the red area).

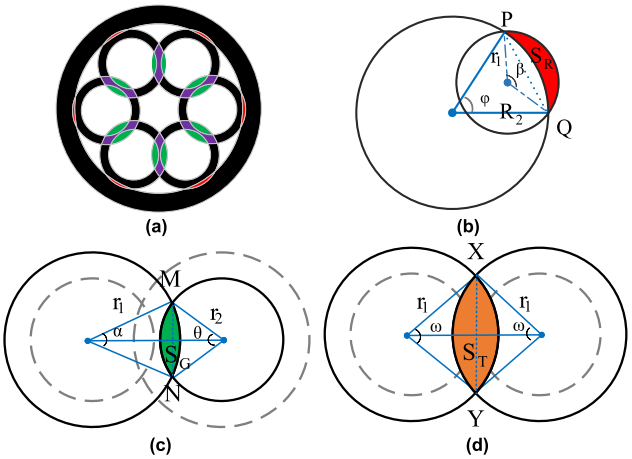

FIGURE 8. (a) The intersected areas of the radiator patch. The geometry of the intersecting area between (b) the main ring and the scaled ring, (c) circles with the radius of r_1 and r_2, and (d) two scaled rings.

S_P can be calculated as follows:

$$S_P = S_T - 2S_G \tag{4}$$

where S_T is the intersecting area between two equal rings with the radius of r_1 and S_G (the green area) is the intersecting area between two circles with the radius of r_1 and r_2. These intersecting areas can be calculated from Fig. 8 (b) to (c) by the following equations.

$$S_R = \frac{1}{2}r_1^2(\varphi - \sin(\varphi)) - \frac{1}{2}R_2^2(\beta - \sin(\beta)) \tag{5}$$

$$\varphi = 2\sin^{-1}(\frac{PQ}{2R_2})\&\beta = 2\sin^{-1}(\frac{PQ}{2r_1}) \tag{6}$$

$$S_G = \frac{1}{2}r_1^2(\alpha - \sin(\alpha)) + \frac{1}{2}r_2^2(\theta - \sin(\theta)) \tag{7}$$

$$\alpha = 2\sin^{-1}(\frac{MN}{2r_1})\&\theta = 2\sin^{-1}(\frac{MN}{2r_2}) \tag{8}$$

$$S_T = r_1^2(\omega - \sin(\omega)) \tag{9}$$

$$\omega = 2\sin^{-1}(\frac{XY}{2r_1}) \tag{10}$$

For the presented antenna, PQ is 1.5812 mm, XY is 2.5278 mm, and MN is 1.6035 mm. So, the intersecting areas are obtained as, $S_R = 0.1068\ mm^2$, $S_T = 1.5545\ mm^2$, $S_G = 0.4333\ mm^2$, and $S_P = 0.6879\ mm^2$. Finally, the effective area and radius of the patch are calculated as follows:

$$A = \pi(6^2 - 5^2) + 6\pi(2^2 - 1.5^2) - 6(0.6879) - 6(0.1068) = 62.7761$$

$$r = \sqrt{\frac{A}{\pi}} = 5.0707\ mm$$

From Equations (2), (3), and the above calculation, f_L will be

$$f_L = \frac{3e^{11}}{2 \times 2.\frac{62.7761}{5.0707}.\sqrt{3.15}} = 3.38GHz$$

As can be deduced from Fig. 3, the theoretical value and the simulated value (3.25 GHz) are approximately equal.

D. PARAMETRIC STUDY

In this section, a parametric study has been performed to provide complete information about the design of the antenna. The effect of four main parameters on the antenna return loss performance is depicted in Figs. 9 and 10. It is seen in Fig. 9 (a) that, for the scaling factor of four, the outer radius of the scaled version is not large enough to create intersecting area. By increasing the scaling factor, the intersected rings provide circular current paths that broaden the bandwidth, especially at the middle frequency.

In Fig 9 (b), the S_{11} curves with various radiuses (R_1, R_2) and the scaling factor $R_1/r_1 = 3$ show by increasing (R_1, R_2) the S_{11} level improves in the frequency range of 7 to 13 GHz by the advent of a new resonant frequency at 10 GHz. As a result, the parametric study on the patch radius shows that $R_1 = 6$ mm and $R_2 = 5$ mm are the optimal radius values to have the largest bandwidth along with impedance matching over UWB frequency range.

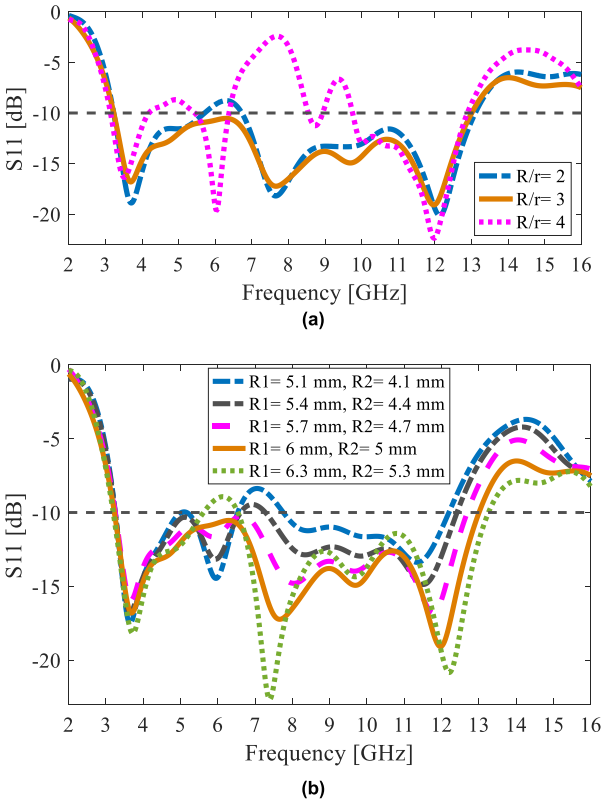

FIGURE 9. Return loss of the final design (Ant. 3) with different values of (a) scaling factor and (b) radius of the rings.

As Fig. 10 (a) shows, the upper frequency of the bandwidth decreases with the increase in the feed width. As can be seen, the best impedance matching and proper impedance bandwidth are obtained at $w_f = 2$ mm. As Fig. 10 (b) demonstrates, the length of the ground plane is a central parameter on antenna return loss performance. By changing the ground plane from 5 mm to 7 mm with a step of 0.5 mm, the value of S_{11} increases in the frequency range of 5.5 to 6.5 GHz and 8 to 10 GHz, while a good impedance matching is achieved in the lower frequencies of the UWB frequency range. Therefore, $h_g = 6$ mm is selected as the optimum length of the ground plane for a bandwidth of 130% (3.25–13 GHz).

E. FREE SPACE MEASUREMENT RESULTS

The photograph of the fabricated antennas is shown in Fig. 11. As Fig. 12 shows, there is an acceptable agreement between the measured and simulated return loss results in free space. The measurement results confirm that the evolution process was reasonable and the final design (via-fed model) is superior to the two other designs. The measured bandwidth of 10 dB return loss for the via-fed antenna is in the range of 3 to 12 GHz. The far-field radiation patterns of the via-fed antenna were measured in an anechoic chamber at frequencies of 4, 7, and 10 GHz. The measured and simulated E-plane (y-z plane) and H-plane (x-z plane) radiation patterns are displayed in Fig. 13 (a) to (c). It can be observed that there is a satisfactory agreement between measurement and

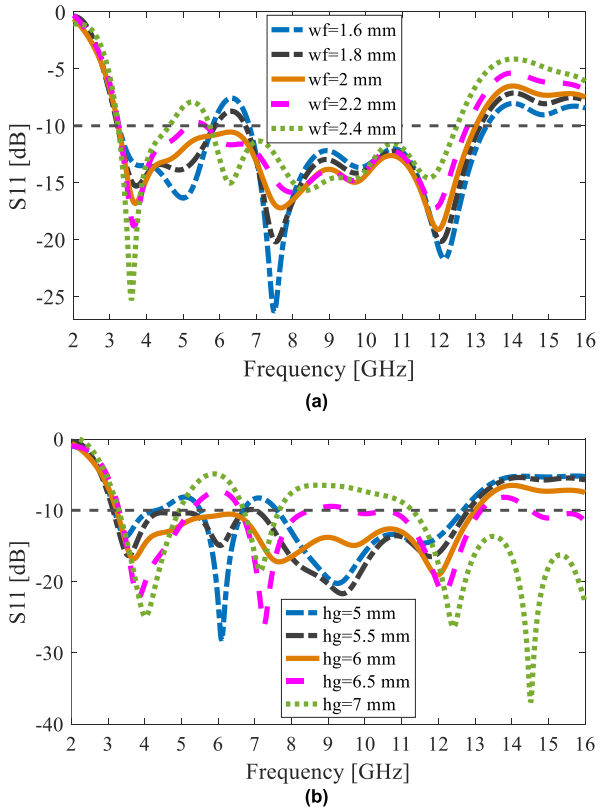

FIGURE 10. Effect of varying (a) feed width and (b) ground plane height on return loss performance of the final design (Ant. 3).

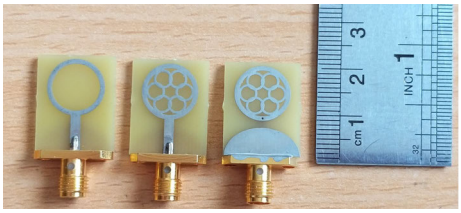

FIGURE 11. Photograph of the fabricated antennas (a) Ant. 1, (b) Ant. 2, and (c) the via-fed antenna (Ant. 3).

simulation results. The radiation characteristics of the via-fed antenna are stable in H-plane over the entire operating frequency range. In other words, the proposed via-fed antenna provides omnidirectional H-plane radiation patterns.

III. EVALUATION FOR APPLICATIONS

A. BAN SYSTEM

In the previous sections, it was demonstrated that the proposed via-fed antenna displays its performance in terms of a promising level of S_{11} and the fidelity factor in the off-body case. To validate that the via-fed antenna is a proper choice in BAN technologies and a promising antenna in wireless data transmission, this section is dedicated to demonstrate the simulation results in the on-body case study. Antennas designed in the BANs must either have a flexible substrate in full contact with the body or be small enough to touch the body on any cross-section. In this case, our antenna has the second feature.

A review of different models of the arm tissue and the reliability of their models regarding their proposed antennas have been discussed [5]. The human arms were modeled in terms of flat, rectangular, and elliptical shapes. In this paper, the human arm tissue consists of the skin, bone, muscle, and fat. As shown in Fig. 14, the proposed model of the human arm is a set of cylinders with a height of 140 mm.

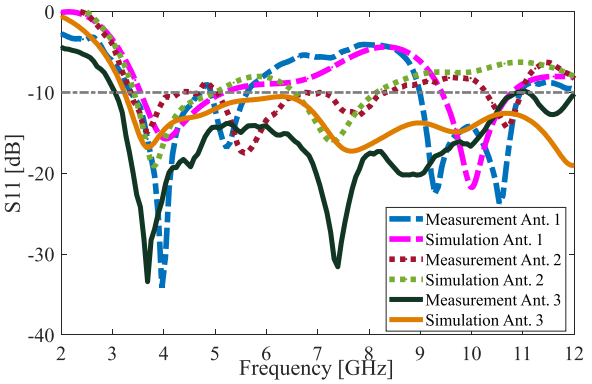

FIGURE 12. Simulated and measured return loss performance of Ant. 1, Ant. 2, and the via-fed UWB antenna in free space.

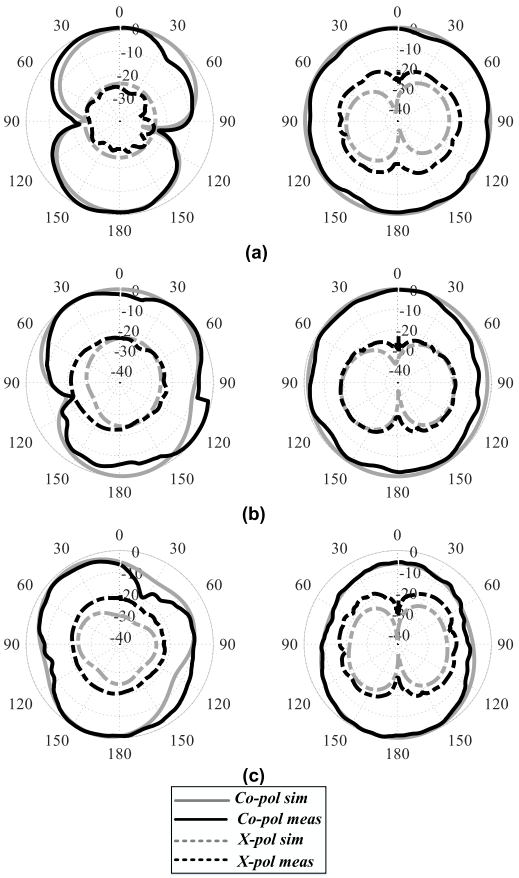

FIGURE 13. Simulated and measured (left) E-plane and (right) H-plane radiation patterns of Ant. 3 at (a) 4, (b) 7, and (c) 10 GHz.

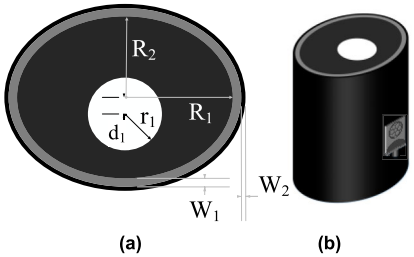

FIGURE 14. (a) Cross section of human arm (b) utilized model of human arm for simulation. $R_1 = 55$ mm, $R_2 = 45$ mm, $r_1 = 17.5$ mm, $d_1 = 4$ mm, $w_1 = 4$ mm, $w_2 = 2$ mm.

The electrical properties of different layers of the human arm are shown in Fig. 15. By considering the dispersion in constitutive parameters of the layers, the human arm model is more precise [34]. The skin layer is shown as the outermost cylinder with an elliptical cross-section, and the fat layer lies immediately below the skin. The arm bone is also modeled as a cylinder that is centered away from the center of the main elliptical cylinder, and the space between the fat and bone layer is filled with muscle.

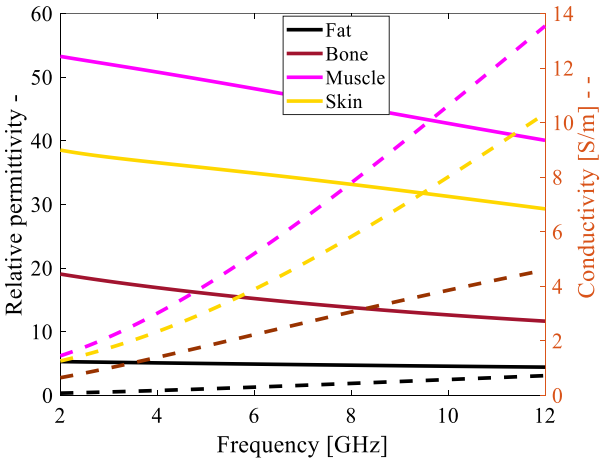

FIGURE 15. Electrical properties of the human arm model, solid lines represent permittivity and dashed lines represent conductivity [34].

Fig. 16 shows the measured and the simulated on-body return loss of the via-fed antenna and the simulated on-body return loss of the second antenna presented in [16]. In both simulation and measurement scenarios, the antennas are directly placed on the tissue without a separation gap. The measurement was carried out where Ant. 3 was in the vicinity of the arm of a female (age = 27, weight = 70 kg, and height = 161 cm). It is apparent that the proposed via-fed antenna preserves its satisfying performance near the human body, and the antenna of [16] does not maintain its UWB functionality in this case. Also, the on-body measured result of Ant. 3 agrees well with the simulated result. The investigation of the fidelity factor of Ant. 3 was performed by 19 virtual probes located in the far-field of the antenna, every 10° from −90° to +90° in both H-plane and E-plane. Fig. 17 represents

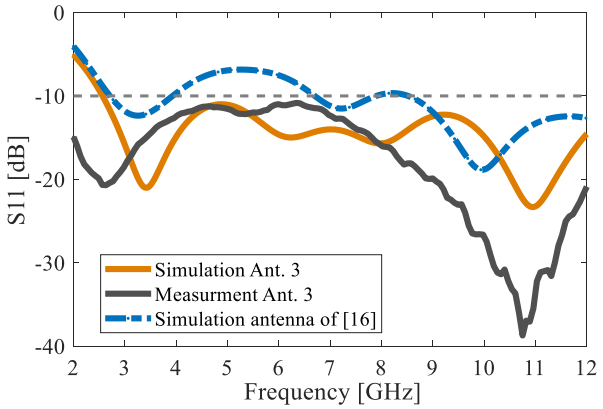

FIGURE 16. Comparison between return loss performance of the proposed via-fed antenna and the antenna of [16] in the vicinity of the human arm.

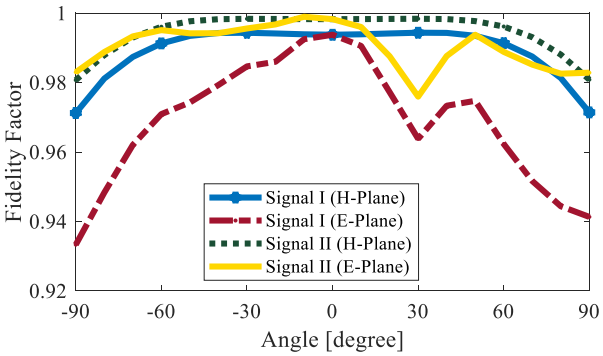

FIGURE 17. Calculated E-plane and H-plane far-field fidelity factor of the proposed via-fed antenna in the vicinity of the arm.

a high fidelity factor between 0.933 and 0.998 that is achieved in the vicinity of the human arm.

The simulated E-plan and H-plane radiation patterns of the via-fed antenna, when placed on the arm, are shown in Fig. 18. Due to the presence of lossy arm tissue and reflections of propagating waves from the arm, the front-to-back ratio is increased. As can be seen, in the on-body case, the via-fed antenna directivity is higher than once it is in free space. Figs. 19 and 20 show a comparison between the signal level of virtual probes when the via-fed antenna is in free space and located on the arm. Considering the H-plane symmetry of the via-fed antenna, only the waveforms at the

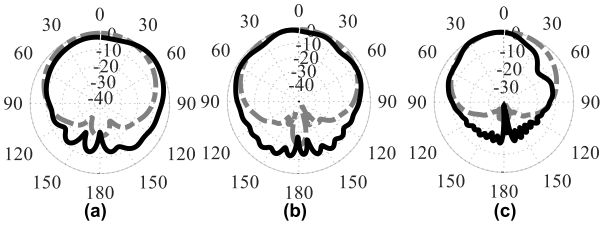

FIGURE 18. Simulated E-plane (solid lines) and H-plane (dashed lines) radiation patterns of Ant. 3 when is placed on the body at (a) 4, (b) 7, and (c) 10 GHz.

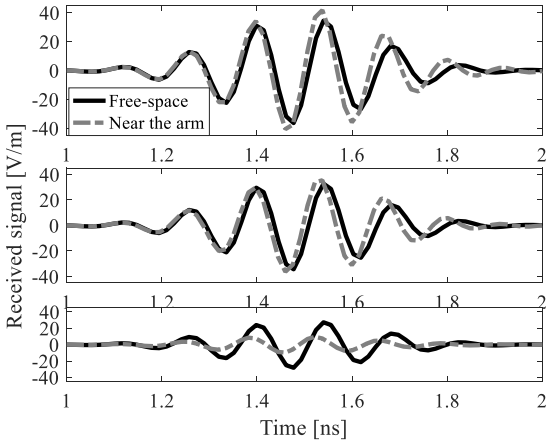

FIGURE 19. H-plane electric-field waveforms at ($\varphi = 0°, \theta = 0°$), ($\varphi = 0°, \theta = +30°$), and ($\varphi = 0°, \theta = +90°$) when Ant. 3 is excited by signal II.

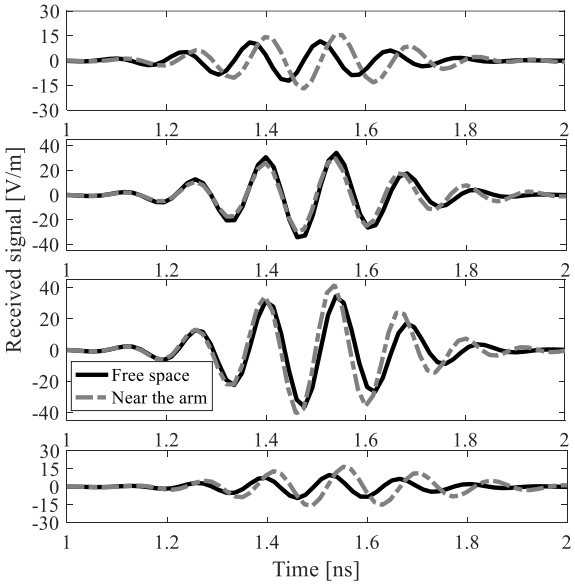

FIGURE 20. E-plane electric-field waveforms at ($\varphi = +90°, \theta = -90°$), ($\varphi = +90°, \theta = -30°$), ($\varphi = +90°, \theta = 0°$), and ($\varphi = +90°, \theta = +90°$) when Ant. 3 is excited by signal II.

positive angles of the H-plane have been plotted. By considering free space and on-body radiation patterns, the difference between the level of the on-body and free space signals is entirely reasonable. The directive nature of on-body electric field patterns causes an increase in the antenna's signal level at $\theta = 0°$ (the first plot of Fig. 19 and the third plot of Fig. 20). As can be seen in Fig. 18, the omnidirectional H-plane radiation pattern changes into a directive one in an on-body case. Hence the decrease in signals' level from $\theta = 0°$ to $\theta = \pm 90°$ is reasonable. Also, Fig. 13 shows that the E-plane radiation patterns in free space are dumbbell-shaped. However, in the on-body case, the level of the E-plane radiation pattern is increased at $\theta = \pm 90°$, which yields a higher level of corresponding on-body signals (the first and last plot of Fig. 20).

B. MICROWAVE IMAGING SYSTEM

In this section, we configured a compact active radar system of 12 antennas in a multi-static configuration to assess the capability of the via-fed antenna on detection and localization for breast cancer applications. A conical model of the breast with 100-mm diameter, a = 0.8b, c = 40 mm, and d = 20 mm is considered (Fig. 21 (a)) [16].

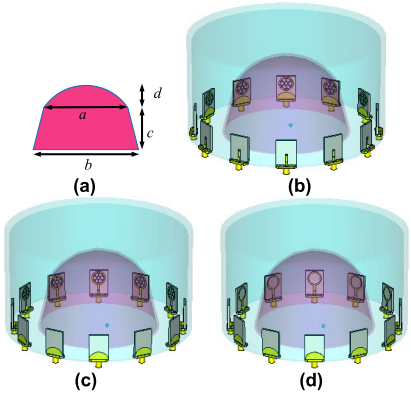

FIGURE 21. (a) Conical model of the breast tissue and the simulation configuration of MI systems (b) Ant. 3, (c) Ant. 2, and (d) Ant. 1.

The electromagnetic properties of the fat tissue are given by the Debye model, $\varepsilon_s = 10$, $\varepsilon_\infty = 7$, $\sigma_s = 0.15$ S/m, $\tau = 7.0ps$ [35]. In addition, the Debye parameters of the symmetric layer of the skin with 2-mm-thickness surrounding the fat tissue are considered as $\varepsilon_s = 39.76$, $\varepsilon_\infty = 15.93$, $\sigma_s = 0.831$ S/m, $\tau = 13.00000\,ps$ [36]. The malignant tumor's electrical properties are assumed to be $\varepsilon_s = 54$, $\varepsilon_\infty = 4$, $\sigma_s = 0.7$ S/m, $\tau = 7.0\ ps$ [35]. According to the simulation model shown in Fig. 21 (b), the antennas are placed in a circular path with a radius of 70 mm at 30-degree increments. Therefore, some sections of the breast are located in the radiating near-field region. As a result, the antenna operates in both the far- and near-fields in the breast imaging system. Consequently, the near-field fidelity factor calculation is necessary for a thorough evaluation of the antenna's performance [29], [31].

As can be seen in Fig. 22, which shows the fidelity factor at the near-field of the via-fed antenna, in both planes, the fidelity factor is greater than 0.97 and 0.92 for Signal II and Signal I inputs, respectively. Fig. 23 shows the fidelity factor over the area of 0 to 45 mm inside the breast. As can be seen, the values are still higher than the accepted fidelity factor for UWB signal transmission.

The MI system is located in a 4 mm thick plastic cylinder with an 80 mm height and 80 mm radius. Also, the cylinder material is R-9807 with the electrical properties of $\varepsilon_r = 1.05$ and $\sigma = 0.00187$ S/m at the middle frequency (5 GHz) [16]. The antenna array and the breast tissue are immersed in a matching liquid with the Debye model of $\varepsilon_s = 4.7077$, $\varepsilon_\infty = 3.1161$, $\sigma_s = 0.496$ S/m, $\tau = 13.00000\,ps$ [36], to mitigate the reflections from the skin.

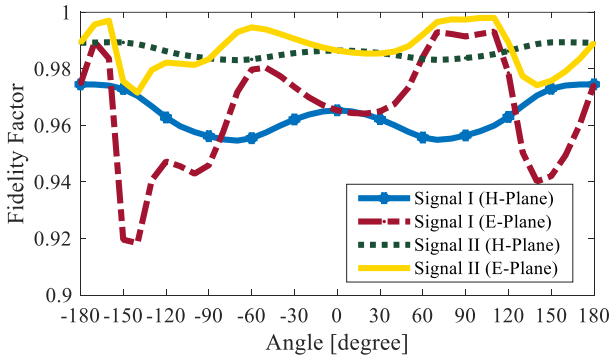

FIGURE 22. Calculated E-plane and H-plane near-field fidelity factor of Ant. 3.

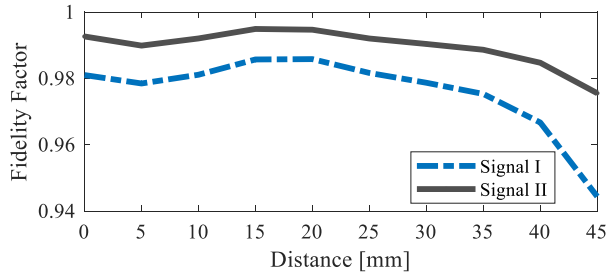

FIGURE 23. Calculated fidelity factor inside the breast tissue.

To investigate the effect of the matching liquid on the return loss performance of the via-fed antenna, a hollow cube with dimensions of 150 × 75 × 150 mm^3 and a wall thickness of 4 mm is simulated. The material of the cube is R-9807 and is filled with the matching liquid while the via-fed antenna is immersed in it. As shown in Fig. 24, Ant. 3 is still matched over the required bandwidth when it is immersed in the matching liquid.

To compare MI results of Ant. 1, Ant. 2, and Ant. 3, two 12-element arrays of Ant. 1 and Ant. 2 with the same properties of our proposed MI system are configured, as shown in Fig. 21 (c) and (d). Individually, each antenna of the array illuminates the breast with a Signal I, and all antennas in the array receive the backscattered signals. In each process, 12 backscattered signals are collected, and this is repeated for another element of the array. After performing the backscattered signals acquisition, the tumor response has to be extracted from the acquired signals. In addition to the tumor's backscattered signals, the received signals contain undesired contents such as antenna coupling, reflections from the skin, and reflections from mechanical parts of the MI system [8]. These undesired signals are the dominant components of the received signals that should be eliminated before applying any algorithm [37]. For subtracting all unwanted signals, [8] utilized the method of antenna array physical rotation. When the antenna array rotates, the unwanted signals such as antenna coupling or skin reflections stay almost identical and appear at the same time position; thus, they can be removed. Our study used the average subtraction method [9], [8]. In this calibration process, primarily,

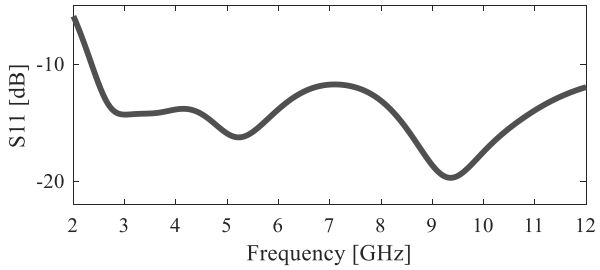

FIGURE 24. The simulated return loss of the via-fed antenna in the presence of the matching liquid.

the antenna coupling and mechanical parts of the MI system were eliminated by subtracting two sets of signals that were obtained from simulations with and without the breast. However, tumor responses are still buried in skin reflections. In the second step, to eliminate skin reflections of the received signals, we form an average of the signals from receivers that have equal angular separation from the transmitter. Subtracting the averaged signal from all of the signals that form this average yields to the tumor's signature and the clutter signals. These proposed methods are based on the assumption that the skin is symmetric.

The present work evaluated the applicability and excellence of our via-fed antenna in breast cancer detection in two scenarios: (1) four simulations of the homogeneous breast tissue with a 3-mm diameter benign tumor (spherical model) located at P(x = 10, y = 10, z = 10) in the configurations of Ant. 1, Ant. 2, the second antenna presented in [16], and Ant. 3, (2) we examined the detection of a malignant tumor model presented in [28], and located at P, with a 40 percent reduction in the average radius. The benign and malignant tumors are shown in Fig. 25.

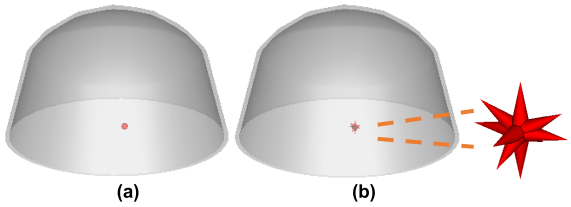

FIGURE 25. (a) The 3-mm diameter spherical benign tumor model (b) the 6-mm average diameter malignant tumor model in a homogenous beast tissue.

Two-dimensional (2D) reconstructed images are generated by applying the delay-and-sum algorithm. Fig. 26 (a) and (b) demonstrate that the tumor's detection is not practicable by applying Ant. 1 and Ant. 2. As can be deduced from the figures, the improving trend of the imaging result through Ant. 1 to Ant. 2 and then to Ant. 3 is quite apparent. It can be seen that in Fig. 26 (c) and (d), we can detect the 3-mm benign tumor by Ant. 3 in the correct location with relatively minor clutter, which cannot be diagnosed by the antenna presented in [16]. This improvement in imaging results originates from the improvement in the fidelity factor

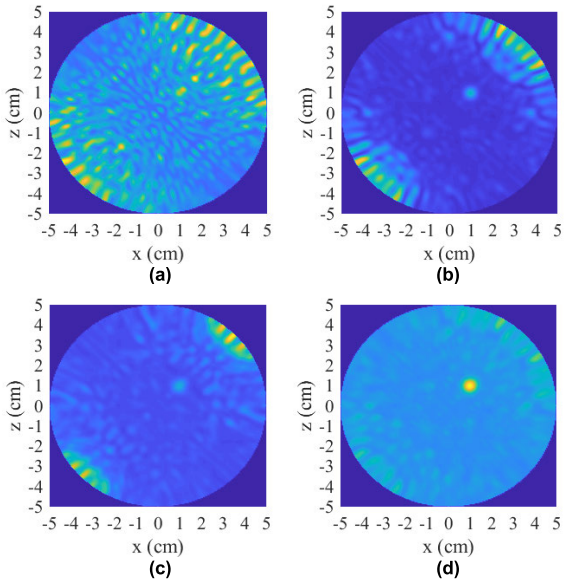

FIGURE 26. Simulation results of a 3-mm diameter spherical benign tumor at P(x = 10, y = 10, z = 10) in the MI systems made by (a) Ant. 1, (b) Ant. 2, (c) the antenna of [16], and (d) Ant. 3.

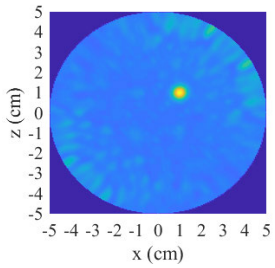

FIGURE 27. Simulation result of the 6-mm average diameter malignant tumor model at P(x = 10, y = 10, z = 10).

at the antenna's final design. The lower the distortion level of the transmitted and received signals are, the more the MI system can detect effectively. We managed to detect the benign tumor 0.25 smaller in size by obtaining a dual-functional high fidelity factor antenna compared with [16]. Fig. 27 shows that our via-fed antenna structure yields the malignant tumor's image accurately at the expected location with relatively insignificant clutter content. Compared with [28], 40 percent smaller malignant and benign tumors are detected through our proposed via-fed antenna.

IV. CONCLUSION

In this paper, a dual-functional, compact, UWB antenna that is suitable for BANs and MI systems was proposed. Aiming at clarifying the capability of the antenna in healthcare applications, the on-body performance and the breast cancer detection were studied and discussed. The fidelity analysis was carried out to study the distortion level in different angular directions for the E-plane as well as the H-plane. Our simulations indicated that the fidelity factor in all directions meets its reasonable criteria in both free space and on-body scenarios. We evaluated the performance of the antenna nearby of a dispersive model of the arm, and the antenna showed satisfactory impedance matching. Exceptional fidelity values greater than 0.93 have been achieved for an on-body scenario. Using this high fidelity factor antenna, we investigated the feasibility of a microwave imaging system in breast cancer detection. A compact array of 12 elements of the via-fed antenna, as an imaging system, was tested and successfully yielded precise detection and localization in two scenarios. Finally, in our imaging system, we diagnosed a 3-mm benign tumor and a malignant tumor with an average radius of 3 mm. The results showed the antenna's promising performance for BANs and MI systems.

REFERENCES

[1] A. Alomainy, A. Sani, A. Rahman, J. G. Santas, and Y. Hao, "Transient characteristics of wearable antennas and radio propagation channels for ultrawideband body-centric wireless communications," *IEEE Trans. Antennas Propag.*, vol. 57, no. 4, pp. 875–884, Apr. 2009.

[2] S. Dey and N. C. Karmakar, "Design of novel super wide band antenna close to the fundamental dimension limit theory," *Sci. Rep.*, vol. 10, no. 1, pp. 1–15, Dec. 2020.

[3] S. A. Hosseini, Z. Atlasbaf, and K. Forooraghi, "A new compact ultra wide band (UWB) planar antenna using glass as substrate," *J. Electromagn. Waves Appl.*, vol. 22, no. 1, pp. 47–59, Jan. 2008.

[4] S. A. Hosseini, Z. Atlasbaf, and K. Forooraghi, "Two new loaded compact palnar ultra-wideband antennas using defected ground structures," *Prog. Electromagn. Res. B*, vol. 2, pp. 165–176, 2008.

[5] M. Koohestani, N. Pires, A. K. Skrivervik, and A. A. Moreira, "Performance Study of a UWB antenna in proximity to a human arm," *IEEE Antennas Wireless Propag. Lett.*, vol. 12, pp. 555–558, 2013.

[6] M. Mahdavi, Z. Atlasbaf, and K. Forooraghi, "A very compact CPW-FED ultra-wideband circular monopole antenna," *Microw. Opt. Technol. Lett.*, vol. 54, no. 7, pp. 1665–1668, Jul. 2012.

[7] B. Yeboah-Akowuah, P. Kosmas, and Y. Chen, "A Q-slot monopole for UWB body-centric wireless communications," *IEEE Trans. Antennas Propag.*, vol. 65, no. 10, pp. 5069–5075, Oct. 2017.

[8] M. Klemm, I. J. Craddock, J. A. Leendertz, A. Preece, and R. Benjamin, "Radar-based breast cancer detection using a hemispherical antenna array—Experimental results," *IEEE Trans. Antennas Propag.*, vol. 57, no. 6, pp. 1692–1704, Jun. 2009.

[9] S. Sadeghi and R. Faraji-Dana, "A practical UBE microwave imaging system using time-domain DORT for tumor detection," *Appl. Comput. Electromagn. Soc. J.*, vol. 31, no. 6, pp. 1–8, 2016.

[10] H. Bahrami, E. Porter, A. Santorelli, B. Gosselin, M. Popović, and L. Rusch, "Flexible sixteen antenna array for microwave breast cancer detection," *IEEE Trans. Biomed. Eng*, vol. 62, no. 10, pp. 2516–2525, May 2015.

[11] A. S. M. Alqadami, N. Nguyen-Trong, B. Mohammed, A. E. Stancombe, M. T. Heitzmann, and A. Abbosh, "Compact unidirectional conformal antenna based on flexible high-permittivity custom-made substrate for wearable wideband electromagnetic head imaging system," *IEEE Trans. Antennas Propag.*, vol. 68, no. 1, pp. 183–194, Jan. 2020.

[12] M. Klemm and G. Troester, "Textile UWB antennas for wireless body area networks," *IEEE Trans. Antennas Propag.*, vol. 54, no. 11, pp. 3192–3197, Nov. 2006.

[13] L. A. Y. Poffelie, P. J. Soh, S. Yan, and G. A. E. Vandenbosch, "A high-fidelity all-textile UWB antenna with low back radiation for off-body WBAN applications," *IEEE Trans. Antennas Propag.*, vol. 64, no. 2, pp. 757–760, Feb. 2016.

[14] R. B. V. B. Simorangkir, A. Kiourti, and K. P. Esselle, "UWB wearable antenna with a full ground plane based on PDMS-embedded conductive fabric," *IEEE Antennas Wireless Propag. Lett.*, vol. 17, no. 3, pp. 493–496, Mar. 2018.

[15] N. Haga, K. Saito, M. Takahashi, and K. Ito, "Characteristics of cavity slot antenna for body-area networks," *IEEE Trans. Antennas Propag.*, vol. 57, no. 4, pp. 837–843, Apr. 2009.

[16] Z. Lasemi and Z. Atlasbaf, "Impact of fidelity factor on breast cancer detection," *IEEE Antennas Wireless Propag. Lett.*, vol. 19, no. 10, pp. 1649–1653, Oct. 2020.
[17] G. Quintero, J. F. Zurcher, and A. K. Skrivervik, "System fidelity factor: A new method for comparing UWB antennas," *IEEE Trans. Antennas Propag.*, vol. 59, no. 4, pp. 2502–2512, Jul. 2011.
[18] E. Pancera, T. Zwick, and W. Wiesbeck, "Spherical fidelity patterns of UWB antennas," *IEEE Trans. Antennas Propag.*, vol. 59, no. 6, pp. 2111–2119, Jun. 2011.
[19] T.-G. Ma and S.-K. Jeng, "Planar miniature tapered-slot-fed annular slot antennas for ultrawide-band radios," *IEEE Trans. Antennas Propag.*, vol. 53, no. 3, pp. 1194–1202, Mar. 2005.
[20] H. Fallahi and Z. Atlasbaf, "Bandwidth enhancement of a CPW-fed monopole antenna with small fractal elements," *AEU Int. J. Electron. Commun.*, vol. 69, no. 2, pp. 590–595, Feb. 2015.
[21] M. Yousefnia, A. Ebrahimzadeh, and M. Dehmollaian, "A time-reversal imaging system for breast screening: Theory and initial phantom results," *IEEE Trans. Biomed. Eng.*, vol. 65, no. 11, pp. 2542–2551, Feb. 2018.
[22] X. Li, S. C. Hagness, M. K. Choi, and D. W. V. D. Weide, "Numerical and experimental investigation of an ultrawideband ridged pyramidal horn antenna with curved launching plane for pulse radiation," *IEEE Antennas Wireless Propag. Lett.*, vol. 2, pp. 259–262, 2003.
[23] J. Bourqui, M. Okoniewski, and E. C. Fear, "Balanced antipodal Vivaldi antenna with dielectric director for near-field microwave imaging," *IEEE Trans. Antennas Propag.*, vol. 58, no. 7, pp. 2318–2326, Jul. 2010.
[24] S. C. Hagness, A. Taflove, and J. E. Bridges, "Three-dimensional FDTD analysis of a pulsed microwave confocal system for breast cancer detection: Design of an antenna-array element," *IEEE Trans. Antennas Propag.*, vol. 47, no. 5, pp. 783–791, May 1999.
[25] S. Latif, D. Flores-Tapia, S. Pistorius, and L. Shafai, "A planar ultrawideband elliptical monopole antenna with reflector for breast microwave imaging," *Microw. Opt. Technol. Lett.*, vol. 56, no. 4, pp. 808–813, Apr. 2014.
[26] M. Bassi, M. Caruso, M. S. Khan, A. Bevilacqua, A. Capobianco, and A. Neviani, "An integrated microwave imaging radar with planar antennas for breast cancer detection," *IEEE Trans. Microw. Theory Techn.*, vol. 61, no. 5, pp. 2108–2118, May 2013.
[27] I. M. Danjuma, M. O. Akinsolu, C. H. See, R. A. Abd-Alhameed, and B. Liu, "Design and optimization of a slotted monopole antenna for ultra-wide band body centric imaging applications," *IEEE J. Electromagn., RF Microw. Med. Biol.*, vol. 4, no. 2, pp. 140–147, Jun. 2020.
[28] H. Zhang, "Microwave imaging for breast cancer detection: The discrimination of breast lesion morphology," *IEEE Access*, vol. 8, pp. 107103–107111, 2020.
[29] A. Akbarpour and S. Chamaani, "Ultrawideband circularly polarized antenna for near-field SAR imaging applications," *IEEE Trans. Antennas Propag.*, vol. 68, no. 6, pp. 4218–4228, Jun. 2020.
[30] M. Sharma, A. Alomainy, and C. Parini, "Fidelity pattern analysis of a CPW-fed miniature UWB antenna using different excitation pulses," *IEEE Antennas Wireless Propag. Lett.*, vol. 14, pp. 494–498, 2015.
[31] A. T. Mobashsher and A. M. Abbosh, "Compact 3-D slot-loaded folded dipole antenna with unidirectional radiation and low impulse distortion for head imaging applications," *IEEE Trans. Antennas Propag.*, vol. 64, no. 7, pp. 3245–3250, Jul. 2016.
[32] K. Bahadori and Y. Rahmat-Samii, "A miniaturized elliptic-card UWB antenna with WLAN band rejection for wireless communications," *IEEE Trans. Antennas Propag.*, vol. 55, no. 11, pp. 3326–3332, Nov. 2007.
[33] W. Balani, M. Sarvagya, A. Samasgikar, T. Ali, and P. Kumar, "Design and analysis of super wideband antenna for microwave applications," *Sensors*, vol. 21, no. 2, p. 477, Jan. 2021.
[34] M. Koohestani, N. Pires, A. K. Skrivervik, and A. A. Moreira, "Influence of the human body on a new coplanar-fed ultra-wideband antenna," in *Proc. 6th Eur. Conf. Antennas Propag. (EUCAP)*, Mar. 2012, pp. 316–319.
[35] E. J. Bond, X. Li, S. C. Hagness, and B. D. Van Veen, "Microwave imaging via space-time beamforming for early detection of breast cancer," *IEEE Trans. Antennas Propag.*, vol. 51, no. 8, pp. 1690–1705, Aug. 2003.
[36] T. Yin, F. H. Ali, and C. C. Reyes-Aldasoro, "A robust and artifact resistant algorithm of ultrawideband imaging system for breast cancer detection," *IEEE Trans. Biomed. Eng.*, vol. 62, no. 6, pp. 1514–1525, Jun. 2015.
[37] Y. Xie, B. Guo, L. Xu, J. Li, and P. Stoica, "Multistatic adaptive microwave imaging for early breast cancer detection," *IEEE Trans. Biomed. Eng.*, vol. 53, no. 8, pp. 1647–1657, Aug. 2006.
[38] E. C. Fear, S. C. Hagness, P. M. Meaney, M. Okoniewski, and M. A. Stuchly, "Enhancing breast tumor detection with near-field imaging," *IEEE Microw. Mag.*, vol. 3, no. 1, pp. 48–56, Mar. 2002.

ZAHRA LASEMIIMENI received the B.Sc. degree in electrical engineering from Babol Noshirvani University of Technology, Babol, Iran, in 2014, and the M.S. degree from Tarbiat Modares University, Tehran, in 2017. Her research interests include antenna design, UWB antennas, healthcare systems, microwave imaging, wireless sensor networks, and body area networks.

ZAHRA ATLASBAF (Senior Member, IEEE) received the B.S. degree in electrical engineering from the University of Tehran, Tehran, Iran, in 1993, and the M.S. and Ph.D. degrees in electrical engineering from Tarbiat Modares University, Tehran, in 1996 and 2002, respectively. She is currently an Associate Professor with the Department of Electrical and Computer Engineering, Tarbiat Modares University. Her current research interests include numerical methods in electromagnetics, theory and applications of metamaterials, microwave, and antenna design, bioelectromagnetic, plasmons, and graphene.

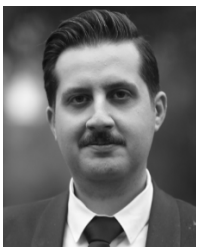

NIMA KARBASCHI received the B.Sc. degree in electrical engineering and the M.Sc. degree in telecommunications engineering from Babol Noshirvani University of Technology, Babol, Iran, in 2014 and 2019, respectively. His research interests include computational electromagnetics, chiral metamaterials, and microwave imaging.